

# A Novel Non-Stationary 6G UAV Channel Model for Maritime Communications

Yu Liu, *Member, IEEE*, Cheng-Xiang Wang, *Fellow, IEEE*, Hengtai Chang, Yubei He, *Student Member, IEEE*, and Ji Bian, *Member, IEEE*

**Abstract**—To achieve space-air-ground-sea integrated communication networks for future sixth generation (6G) communications, unmanned aerial vehicle (UAV) communications applying to maritime scenarios serving as mobile base stations have recently attracted more attentions. The UAV-to-ship channel modeling is the fundamental for the system design, testing, and performance evaluation of UAV communication systems in maritime scenarios. In this paper, a novel non-stationary multi-mobility UAV-to-ship channel model is proposed, consisting of three kinds of components, i.e., the line-of-sight (LoS) component, the single-bounce (SB) components resulting from the fluctuation of sea water, and multi-bounce (MB) components introduced by the waveguide effect over the sea surface. In the proposed model, the UAV as the transmitter (Tx), the ship as the receiver (Rx), and the clusters between the Tx and Rx, can be seen as moving with arbitrary velocities and arbitrary directions. Then, some typical statistical properties of the proposed UAV-to-ship channel model, including the temporal autocorrelation function (ACF), spatial cross-correlation function (CCF), Doppler power spectrum density (PSD), delay PSD, angular PSD, stationary interval, and root mean square (RMS) delay spread, are derived and investigated. Finally, by comparing with the available measurement data, the accuracy of proposed channel model is validated.

**Index Terms**—6G, UAV channels, maritime communications, non-stationarity, multi-mobility, channel statistical properties.

## I. INTRODUCTION

This work was supported by the National Key R&D Program of China under Grant 2018YFB1801101, the National Natural Science Foundation of China (NSFC) under Grants 61960206006 and 62001269, the Frontiers Science Center for Mobile Information Communication and Security, the High Level Innovation and Entrepreneurial Research Team Program in Jiangsu, the High Level Innovation and Entrepreneurial Talent Introduction Program in Jiangsu, the Research Fund of National Mobile Communications Research Laboratory, Southeast University, under Grant 2020B01, the Fundamental Research Funds for the Central Universities under Grant 2242020R30001, the EU H2020 RISE TESTBED2 project under Grant 872172, the Taishan Scholar Program of Shandong Province, the Shandong Natural Science Foundation under Grants ZR2019BF04 and ZR2020QF001, and the Fundamental Research Funds of Shandong University under Grant 2020GN032.

Y. Liu is with School of Microelectronics, Shandong University, Jinan, 250101, China (e-mail: yuliu@sdu.edu.cn).

C.-X. Wang (corresponding author) is with the National Mobile Communications Research Laboratory, School of Information Science and Engineering, Southeast University, Nanjing, 210096, China, and also with Purple Mountain Laboratories, Nanjing, 211111, China (e-mail: chxwang@seu.edu.cn).

H. Chang and Y. He are with Shandong Provincial Key Lab of Wireless Communication Technologies, School of Information Science and Engineering, Shandong University, Qingdao, 266237, China (e-mail: hunter\_chang@126.com, heyubei@126.com).

J. Bian is with School of Information Science and Engineering, Shandong Normal University, Jinan, 250358, China (e-mail: jibian@sdu.edu.cn).

WITH the rapid developments of unmanned aerial vehicle (UAV) communications in maritime scenarios, the vast high-reliable and low-delay transmission of UAV related sensing and computing data are required [1], [2]. Therefore, future UAV communication systems are hoped to be integrated into sixth generation (6G) cellular networks to realize high-speed data transmission [3]–[5]. Due to the enormous potential of UAV communication applications in maritime environments, the underlying wireless channels, i.e., UAV-to-ship channels, should be fully investigated and the corresponding channel model should be developed. An accurate and general UAV-to-ship channel model is indispensable for communication algorithm and system design. For instance, the reproduction of dynamic UAV communication scenario can verify the performance of UAV trajectory optimization algorithm. The effective system testing can be conducted for the emerging UAV-to-ship technologies and network architecture [3]. Different from the communication environments of terrestrial scenarios, the UAV communication in maritime scenario has some unique channel characteristics, such as irregular fluctuation of sea surface caused by sea water fluctuation, the signal attenuation caused by sea climate change, and the waveguide effect caused by the humidity, pressure, and temperature of troposphere over the sea [6]. Compared with UAV-to-ground channels, the scatterers in UAV-to-ship channels are in irregular motion because of sea waves. Moreover, the waveguide propagation is an important propagation mechanism in UAV-to-ship channels, which will lead to different channel properties. To better develop the future UAV communication system in maritime scenarios, the related channel modeling is essential [7], [8].

In the open literature, existing channel modeling for maritime communications can be classified as channel measurements and theoretical modeling [9]. A series of UAV-based channel measurement campaigns at L-band and C-band have been conducted and the related channel models have been proposed [10]–[13]. In [10] and [11], some initial results on air-ground channel measurements and modeling for over-sea setting were introduced. The measurement equipment was placed in a coastal setting as transmitter (Tx), and the flight was over the Pacific Ocean as receiver (Rx). Based on the measurements, the channel impulse responses (CIRs) were obtained, and some channel statistics for different flight paths and frequency bands were analyzed, such as power delay profile (PDP), path loss, and delay spreads. In order to explore the channel characteristics of air-to-air scenarios, the channel measurements in Hawaii were carried out using 2.3 GHz

frequency with a 20 MHz bandwidth. By analyzing the measured CIRs, it showed that channel model over the sea can be described as a 2-ray model, which was composed of direct path and specular path reflecting from the sea [14]. By conducting a dual-band measurement campaign for over-water scenario, the path loss models and wideband channel models were further developed in [12]. The analysis results showed that a third ray which appeared intermittently, should be added in the 2-ray model to better describe the over-water environments. In [13], dual-band air-ground channel measurements for over harbor environment were reported. The measured results showed that the path loss in these two bands is larger than free space case, and the amplitude fading is faster than Rayleigh model. The number of multipath and their delays in the blacklobe and main beam cases were also compared and analyzed. Beyond these, the probability of the occurrence of multipath for air-ground channel over sea surface was introduced in [15]. Based on the UAV channel measurements conducting at C-band, the multipath statistics at different low airborne altitudes were further investigated, and the influences of the evaporation and elevated ducts on the over-water communication link were analyzed. The existence of the evaporation and elevated ducts was found to decrease the propagation loss over the sea surface. A further study of ducting effects on air-ground over sea propagations was presented in [16]. The observation results showed the evaporation and elevated ducts can greatly improve over sea air-ground propagations. The aforementioned channel measurements are focused on the sub-6 GHz frequency bands. For better integrating into beyond fifth generation (B5G) communications, the channel modeling for UAV communication in mmWave bands was given by using the ray tracing method [17]. Based on the simulation results, the received signal strength and delay spreads of multipath for different flight heights in different scenarios were primarily analyzed. In [18], an improved spatial partitioning ray tracing method was proposed to model the channel between UAV and boat, and the channel characteristics including the channel scattering function and the PDP were analyzed. But in the simulations, the movements of UAV and boat were not considered, and the ray tracing modeling methods have a high computational complexity. In [19], the finite-difference time domain (FDTD) modeling method was used to model the channel between the UAV and vessels during sea surface communications. For each modeling simulation, a random sea surface was produced. The Tx was set as 40 m high than the sea surface, and the Rx was set close to the surface. The simulation results showed that resulting from the reflections of rough sea surface, the propagations between the UAV and vessels should be complex multipath components rather than 2-ray or 3-ray model. However, the influence of duct effect on the channel model was ignored due to the difficult combination of duct effect and FDTD model. Most of the aforementioned channel measurements and models are mainly focused on the study of large-scale fading, and simplified analysis of small-scale fading characteristics. In [20], air-ground UAV channel measurements at 1 GHz and 4 GHz were provided. Based on the measurement data, the comprehensive

large-scale and small-scale channel characteristics were further investigated. In [21], UAV channel measurements considering 5 horizontal and 5 vertical UAV flight routes were carried out, and more channel characteristics such as path loss and fast fading were thoroughly studied. By taking the non-stationary channel characteristics into account, a three dimensional (3D) geometry-based stochastic model for UAV communications was proposed in [22], and a novel 6G UAV channel model was provided in [23] and [24]. During the channel modeling, the movements of Tx and Rx were both considered, and the non-stationarities in different domains of channels were also involved [25]. These channel models can better mimic the UAV-to-ground channel characteristics [26]–[28], but cannot describe the propagation characteristics in maritime scenarios [29], [30]. The existing standardized channel models, such as 3GPP-like geometry-based model have not covered the UAV-to-ship scenarios. In fact, the communication environments of maritime scenarios are very different from those of terrestrial scenarios, as well as the channel propagation characteristics. In the modeling of UAV-to-ship scenarios, the depiction of propagation environment, such as sea wave fluctuation and ducting mechanisms should be introduced.

To the best of the authors' knowledge, accurate UAV channel models for the maritime scenarios, which consider the irregular fluctuation of sea surface caused by sea water fluctuation, the signal attenuation caused by sea climate change, and the waveguide effect caused by sea atmosphere, are still missing from the literature. Current UAV channel modeling works for maritime communications are in the early stage, and limited on studies of related channel properties. This paper aims to propose a novel 6G UAV-to-ship channel model, which can mimic the unique channel characteristics. The novelties are listed as follows.

- (1) Our research works firstly propose a novel UAV-to-ship channel model for maritime communications considering multi-mobility, and focus on studying the typical small-scale fading channel properties.
- (2) Due to the irregular fluctuation of sea surface and the weather variation over time, the proposed model introduces the wave equation of sea surface. The single-cluster model is used to describe the scatterers distribution from sea surface, and the birth-death process and wave equation are combined to describe clusters evolutions.
- (3) For the UAV-to-ship transmission in maritime scenarios, the evaporation duct and elevated duct over the sea surface are considered. The twin-cluster model is used to describe the waveguide effect, which can be modeled by several-order reflections to mimic the signal propagations between the two clusters.
- (4) The channel model considering the multi-mobility of UAV and ship with arbitrary speeds and moving directions is given. The related channel properties in different moving speeds and directions are further investigated.

The remainder of this paper is structured as follows. In Section II, the 3D non-stationary UAV-to-ship channel model for maritime communications is introduced. Section III analyzes the

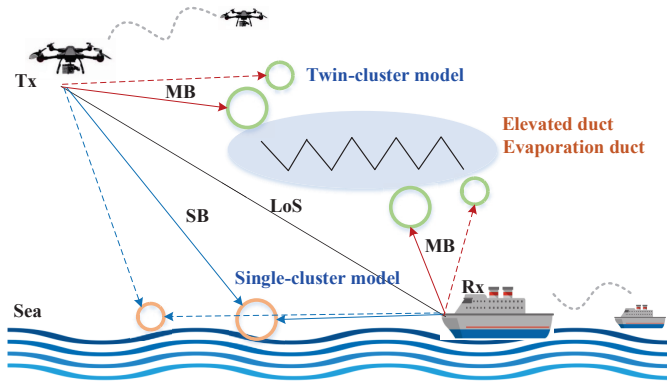


Fig. 1. Description of UAV-to-ship network architecture for maritime scenarios.

channel statistical properties. Results and discussion are given in Section IV. Finally, conclusions are drawn in Section V.

## II. UAV-TO-SHIP CHANNEL MODEL FOR MARITIME COMMUNICATIONS

A brief description of UAV-to-ship communication network architecture for maritime scenarios is shown in Fig. 1. The UAV side is set as the Tx, and the ship side is set as the Rx. Multiple antennas can be deployed on two sides respectively. The UAV-to-ship communication frequencies mainly adopt sub-6 GHz, and can also be extended to mmWave bands to be better integrated into the future 6G networks [31], [32]. Due to the fluctuation of sea water, the rough sea surface will bring more reflections and cause multipath fading [15]. Moreover, the evaporation and elevated ducts over the sea surface will influence the wireless propagations between the UAV and ship [6], [16]. At this point, the waveguide effect over sea should be considered. Therefore, the whole communication link can contain three parts: the line-of-sight (LoS) component denotes that UAV communicating with ship directly. The single-cluster model means that the received signals can arrive at the ship by one reflection from the rough sea surface, which can be described by single-bounce (SB) component. The twin-cluster model denotes that the received signals experience the ducting effects and/or adverse weather effects during the propagations, which can be abstracted as multi-bounce (MB) components. In the entire communication process, the UAV and ship can both be set as moving along arbitrary directions with arbitrary moving speeds, and the antennas deployed on the both sides can also rotate discretionarily [33], [34].

Based on the UAV-to-ship communication architecture, a novel 3D non-stationary channel model which can mimic the UAV channel propagation characteristics is presented in Fig. 2. The Tx (UAV) and Rx (ship) sides are equipped with  $P$  and  $Q$  antenna elements, respectively. The proposed channel model consists of LoS, SB, and MB cases [35], [36]. For simplicity, only the  $k$ th cluster in SB case is illustrated, where the  $K$  is the number of single-cluster. Moreover, the  $n$ th cluster pair in MB is given in detail, where  $N$  is the number of twin-cluster. Each cluster or

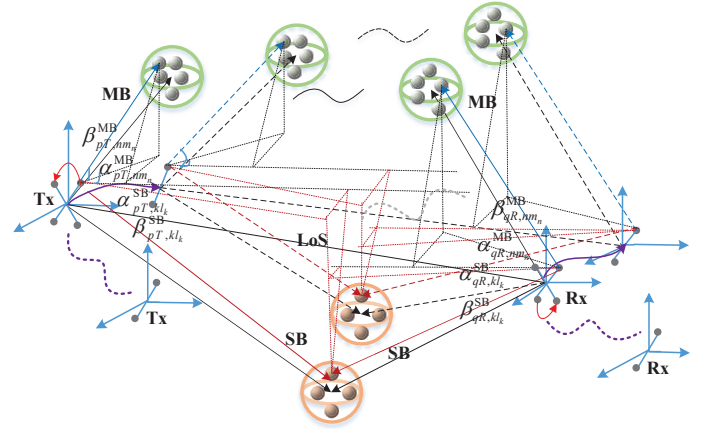


Fig. 2. A 3D non-stationary dual-mobility UAV channel model for maritime communications.

cluster pair can be moving with certain probability. In the SB case, the clusters are randomly produced and moving with the fluctuation of sea surface. In the MB case, the  $n$ th twin-cluster can be represented as  $C_{n,A}$  and  $C_{n,Z}$ . On one hand, the propagation space between the first bounce  $C_{n,A}$  and the last bounce  $C_{n,Z}$  can be described by the waveguide effect. On the other hand, the propagation space can also be abstracted as virtual link to depict the influence of severe weather. All parameters in the channel model are established as time-variant. The corresponding parameters involved in the UAV-to-ship channel modeling are defined in Table I. The proposed channel model is applicable for sub-6 GHz UAV-to-ship communication scenario. Regarding the maritime environment properties, the proposed model supports channel simulation considering the motions of UAV, ship, and scatterers between the UAV and ship, according to the environment parameters such as wind speed.

### A. Descriptions of Theoretical and Simulation Models

In this part, the 3D non-stationary theoretical channel model considering the mobilities of Tx, Rx, and clusters is presented. The complex CIR of total components can be expressed as

$$\begin{aligned}
 h_{pq}^{tot}(t, \tau) = & \eta_1 \sqrt{\frac{K_{pq}(t)}{K_{pq}(t)+1}} h_{pq}^{LoS}(t) \delta(\tau - \tau^{LoS}(t)) \\
 & + \eta_2 \sqrt{\frac{1}{K_{pq}(t)+1}} \sum_{k=1}^{K(t)} \sum_{l_k=1}^{L_k} h_{pq,kl_k}^{SB}(t) \delta(\tau - \tau_{l_k}^{SB}(t)) \\
 & + \eta_3 \sqrt{\frac{1}{K_{pq}(t)+1}} \sum_{n=1}^{N(t)} \sum_{m_n=1}^{M_n} h_{pq,nm_n}^{MB}(t) \delta(\tau - \tau_{m_n}^{MB}(t))
 \end{aligned} \quad (1)$$

where  $\eta_1$ ,  $\eta_2$ , and  $\eta_3$  denote the proportions of LoS, SB, and MB components.  $K(t)$  is the number of SB clusters, and  $L_k$  is the number of rays inside the  $k$ th cluster.  $N(t)$  is the number of MB clusters, and  $M_n$  is the number of rays inside the  $n$ th cluster.  $K_{pq}(t)$  is the K factor. The delay of LoS path between the  $p$ th Tx and  $q$ th Rx can be expressed as

$$\tau^{LoS}(t) = \frac{\|D_{pq}^{LoS}(t)\|}{c} \quad (2)$$

TABLE I  
DEFINITION OF PARAMETERS.

Parameters	Definition
$\alpha_{pT,kl_k}^{SB}, \beta_{pT,kl_k}^{SB}$	The AAoD and EAoD of the $l_k$ th ray of $k$ th cluster in SB case
$\alpha_{qR,kl_k}^{SB}, \beta_{qR,kl_k}^{SB}$	The AAoA and EAoA of the $l_k$ th ray of $k$ th cluster in SB case
$\alpha_{pT,nm_n}^{MB}, \beta_{pT,nm_n}^{MB}$	The AAoD and EAoD of the $m_n$ th ray of $n$ th cluster in MB case
$\alpha_{qR,nm_n}^{MB}, \beta_{qR,nm_n}^{MB}$	The AAoA and EAoA of the $m_n$ th ray of $n$ th cluster in MB case
$D_{pq}^{LoS}$	The distance from $p$ th Tx to $q$ th Rx
$D_{pT,kl_k}^{SB}, D_{qR,kl_k}^{SB}$	The distance from $p$ th Tx/ $q$ th Rx to cluster $C_k$ via the $l_k$ th ray of $k$ th cluster in SB case
$D_{pT,nm_n}^{MB}, D_{qR,nm_n}^{MB}$	The distance from $p$ th Tx/ $q$ th Rx to cluster $C_{n,A}/C_{n,Z}$ via the $m_n$ th ray of $n$ th cluster in MB case
$f_{pT,kl_k}^{SB}, f_{qR,kl_k}^{SB}$	The Doppler frequency of $p$ th Tx/ $q$ th Rx via $l_k$ th ray of $k$ th cluster in SB case
$f_{pT,nm_n}^{MB}, f_{qR,nm_n}^{MB}$	The Doppler frequency of $p$ th Tx/ $q$ th Rx via $m_n$ th ray of $n$ th cluster in MB case
$M_V^T, M_V^R$	The antenna rotation matrix vectors of Tx/Rx unit
$\phi_{A,V}^T, \phi_{E,V}^T$	The antenna rotation azimuth and elevation angles of Tx antenna
$\phi_{A,V}^R, \phi_{E,V}^R$	The antenna rotation azimuth and elevation angles of Rx antenna
$v^{UAV}, v^{Ship}$	The moving speeds of UAV and ship
$a^{UAV}, a^{Ship}$	The accelerated speeds of UAV and ship
$v^{SB}, a^{SB}$	The moving speed and accelerated speed of cluster $C_k$ in SB case
$v_{CA}^{MB}, v_{CZ}^{MB}$	The moving speed of cluster $C_{n,A}/C_{n,Z}$ in MB case
$a_{CA}^{MB}, a_{CZ}^{MB}$	The accelerated speed of cluster $C_{n,A}/C_{n,Z}$ in MB case
$\phi_{A,UAV}, \phi_{E,UAV}$	The azimuth and elevation angles of UAV along the moving direction
$\phi_{A,Ship}, \phi_{E,Ship}$	The azimuth and elevation angles of ship along the moving direction
$\omega_{A,UAV}, \omega_{E,UAV}$	The azimuth and elevation angular speed of UAV along the moving direction
$\omega_{A,Ship}, \omega_{E,Ship}$	The azimuth and elevation angular speed of ship along the moving direction
$\lambda_G, \lambda_R$	The generation rate and recombination rate of cluster

where  $c$  is the speed of light.

The SB delay between the  $p$ th Tx and  $q$ th Rx via the  $l_k$ th ray of  $k$ th single-cluster can be expressed as

$$\tau_{l_k}^{SB}(t) = \frac{\|D_{pT,kl_k}^{SB}(t)\| + \|D_{qR,kl_k}^{SB}(t)\|}{c}. \quad (3)$$

The MB delay between the  $p$ th Tx and  $q$ th Rx via the  $m_n$ th ray of  $n$ th twin-cluster can be expressed as

$$\tau_{m_n}^{MB}(t) = \frac{\|D_{pT,nm_n}^{MB}(t)\| + \|D_{qR,nm_n}^{MB}(t)\|}{c} + \tau_{wg}(t). \quad (4)$$

-In the LoS case

The channel gain  $h_{pq}^{LoS}(t)$  can be expressed as

$$h_{pq}^{LoS}(t) = \begin{bmatrix} F_{p,V}^T(\alpha_{pT}^{LoS}(t), \beta_{pT}^{LoS}(t)) \\ F_{p,H}^T(\alpha_{pT}^{LoS}(t), \beta_{pT}^{LoS}(t)) \\ 0 \\ 0 \end{bmatrix}^T \begin{bmatrix} F_{q,V}^R(\alpha_{qR}^{LoS}(t), \beta_{qR}^{LoS}(t)) \\ F_{q,H}^R(\alpha_{qR}^{LoS}(t), \beta_{qR}^{LoS}(t)) \end{bmatrix} \times e^{j2\pi \int_0^t f_{pq}^{LoS}(t) dt} \cdot e^{j\frac{2\pi}{\lambda}(\mathbf{d}_p^T(t) \cdot \mathbf{M}_V^T(t) \cdot \Phi_{LoS}^T(t) + \mathbf{d}_q^R(t) \cdot \mathbf{M}_V^R(t) \cdot \Phi_{LoS}^R(t))}. \quad (5)$$

For the LoS case,  $\alpha_{pT}^{LoS}(t)$ ,  $\beta_{pT}^{LoS}(t)$ ,  $\alpha_{qR}^{LoS}(t)$ , and  $\beta_{qR}^{LoS}(t)$  denote the the azimuth angle of departure (AAoD), the elevation angle of departure (EAoD), the azimuth angle of arrival (AAoA), and the elevation angle of arrival (EAoA) of LoS component, respectively.  $\Theta_{pT}^{LoS}$  is the initial phase. The angle vectors  $\Phi_{LoS}^T(t)$  and  $\Phi_{LoS}^R(t)$  are composed of the AoDs and

AoAs in LoS case. Functions  $F_{p,V}^T(\cdot)$ ,  $F_{p,H}^T(\cdot)$ ,  $F_{q,V}^R(\cdot)$ ,  $F_{q,H}^R(\cdot)$  denote the antenna patterns of Tx and Rx. The time-variant Doppler frequency is denoted by  $f_{pq}^{LoS}(t)$ . The rotation matrices for the Tx array  $\mathbf{M}_V^T(t)$  and the Rx array  $\mathbf{M}_V^R(t)$  can be expressed as (6). The angles  $\phi_{A,V}^{T(R)}(t)$  and  $\phi_{E,V}^{T(R)}(t)$  denote the azimuth and elevation rotation angles of the Tx/Rx antennas array. Moreover, the location vectors  $\mathbf{d}_p^T(t) = [x_p^T(t), y_p^T(t), z_p^T(t)]$  and  $\mathbf{d}_q^R(t) = [x_q^R(t), y_q^R(t), z_q^R(t)]$  are the 3D locations of the  $p$ th Tx and  $q$ th Rx antennas.

-In the SB case

The channel coefficient  $h_{pq,kl_k}^{SB}(t)$  can be given by

$$h_{pq,kl_k}^{SB}(t) = \begin{bmatrix} F_{p,V}^T(\alpha_{pT,kl_k}^{SB}(t), \beta_{pT,kl_k}^{SB}(t)) \\ F_{p,H}^T(\alpha_{pT,kl_k}^{SB}(t), \beta_{pT,kl_k}^{SB}(t)) \end{bmatrix}^T \begin{bmatrix} \sqrt{\kappa_{k,l_k}^{-1}} e^{j\Theta_{k,l_k}^{VV}} & e^{j\Theta_{k,l_k}^{HV}} \\ e^{j\Theta_{k,l_k}^{HV}} & \sqrt{\kappa_{k,l_k}^{-1}} e^{j\Theta_{k,l_k}^{VV}} \end{bmatrix} \begin{bmatrix} F_{q,V}^R(\alpha_{qR,kl_k}^{SB}(t), \beta_{qR,kl_k}^{SB}(t)) \\ F_{q,H}^R(\alpha_{qR,kl_k}^{SB}(t), \beta_{qR,kl_k}^{SB}(t)) \end{bmatrix} e^{j\varphi_{kl_k}^{SB}} \times e^{j2\pi \int_0^t (f_{pT,kl_k}^{SB}(t) + f_{qR,kl_k}^{SB}(t)) dt} \times e^{j\frac{2\pi}{\lambda}(\mathbf{d}_p^T(t) \cdot \mathbf{M}_V^T(t) \cdot \Phi_{pT,kl_k}^{SB}(t) + \mathbf{d}_q^R(t) \cdot \mathbf{M}_V^R(t) \cdot \Phi_{qR,kl_k}^{SB}(t))}. \quad (7)$$

For the SB component,  $f_{pT,kl_k}^{SB}(t)$  and  $f_{qR,kl_k}^{SB}(t)$  are the time-variant Doppler frequencies caused by the movements of  $p$ th Tx and  $q$ th Rx antennas elements, and  $\Phi_{pT(qR),kl_k}^{SB}(t)$  denotes the time-variant AoDs/AoAs vector between the  $l_k$ th scatterer in the

$$\mathbf{M}_V^{T(R)}(t) = \begin{bmatrix} \cos(\phi_{E,V}^{T(R)}(t)) \cos(\phi_{A,V}^{T(R)}(t)) & -\sin(\phi_{A,V}^{T(R)}(t)) & -\sin(\phi_{E,V}^{T(R)}(t)) \cos(\phi_{A,V}^{T(R)}(t)) \\ \cos(\phi_{E,V}^{T(R)}(t)) \sin(\phi_{A,V}^{T(R)}(t)) & \cos(\phi_{A,V}^{T(R)}(t)) & -\sin(\phi_{E,V}^{T(R)}(t)) \sin(\phi_{A,V}^{T(R)}(t)) \\ \sin(\phi_{E,V}^{T(R)}(t)) & 0 & \cos(\phi_{E,V}^{T(R)}(t)) \end{bmatrix}^T. \quad (6)$$

$k$ th single-cluster and Tx/Rx.  $\kappa_{k,l_k}^{-1}$  is the cross polarization power ratio. The corresponding expressions can be calculated as

$$\Phi_{pT(qR),kl_k}^{SB}(t) = \begin{bmatrix} \cos(\beta_{pT(qR),kl_k}^{SB}(t)) \cos(\alpha_{pT(qR),kl_k}^{SB}(t)) \\ \cos(\beta_{pT(qR),kl_k}^{SB}(t)) \sin(\alpha_{pT(qR),kl_k}^{SB}(t)) \\ \sin(\beta_{pT(qR),kl_k}^{SB}(t)) \end{bmatrix}^T \quad (8)$$

$$f_{pT,kl_k}^{SB}(t) = \frac{\langle \mathbf{D}_{pT,kl_k}^{SB}(t), \mathbf{v}^{UAV}(t) - \mathbf{v}^{SB}(t) \rangle}{\lambda \|\mathbf{D}_{pT,kl_k}^{SB}(t)\|} \quad (9)$$

$$f_{qR,kl_k}^{SB}(t) = \frac{\langle \mathbf{D}_{qR,kl_k}^{SB}(t), \mathbf{v}^{Ship}(t) - \mathbf{v}^{SB}(t) \rangle}{\lambda \|\mathbf{D}_{qR,kl_k}^{SB}(t)\|} \quad (10)$$

where

$$\mathbf{D}_{pT,kl_k}^{SB}(t) = \mathbf{D}_{pT,kl_k}^{SB}(t_0) + \mathbf{D}_C^{SB}(t) - \mathbf{D}^{UAV}(t) \quad (11)$$

$$\mathbf{D}_{qR,kl_k}^{SB}(t) = \mathbf{D}_{qR,kl_k}^{SB}(t_0) + \mathbf{D}_C^{SB}(t) - \mathbf{D}^{Ship}(t) \quad (12)$$

$$\mathbf{D}_C^{SB}(t) = \int_0^t \mathbf{v}^{SB}(t) dt = \int_0^t (\mathbf{v}^{SB}(t_0) + a^{SB} \cdot t) dt \quad (13)$$

$$\begin{aligned} \mathbf{D}^{UAV/Ship}(t) &= \int_0^t \mathbf{v}^{UAV/Ship}(t) dt \\ &= \int_0^t (\mathbf{v}^{UAV/Ship}(t_0) + a^{UAV/Ship} \cdot t) dt. \end{aligned} \quad (14)$$

Here,  $\mathbf{D}_{pT,kl_k}^{SB}(t)$  stands for the time-variant distance from the  $p$ th Tx antenna unit to the  $k$ th single-cluster via the  $l_k$ th ray, and  $\mathbf{D}_{qR,kl_k}^{SB}(t)$  stands for the time-variant distance from the  $k$ th single-cluster to the  $q$ th Rx antenna unit via the  $l_k$ th ray. The distance vector  $\mathbf{D}_{pT,kl_k}^{SB}(t)$  can be obtained by the initial distance vector at Tx  $\mathbf{D}_{pT,kl_k}^{SB}(t_0)$ , the moving distance vector of single-cluster  $\mathbf{D}_C^{SB}(t)$ , and the moving distance vector of UAV  $\mathbf{D}^{UAV}(t)$ . Moreover, the distance vector  $\mathbf{D}_{qR,kl_k}^{SB}(t)$  can be acquired by the initial distance vector at Rx  $\mathbf{D}_{qR,kl_k}^{SB}(t_0)$ , the moving distance vector of single-cluster  $\mathbf{D}_C^{SB}(t)$ , and the moving

distance vector of ship  $\mathbf{v}^{UAV/Ship}$ . The moving speed vectors of UAV, single-cluster, and ship can be expressed as

$$\begin{aligned} \mathbf{v}^{UAV/SB/Ship}(t) &= |\mathbf{v}^{UAV/SB/Ship}(t)| \\ &\times \begin{bmatrix} \cos(\phi_{E,UAV/SB/Ship}(t)) \cos(\phi_{A,UAV/SB/Ship}(t)) \\ \cos(\phi_{E,UAV/SB/Ship}(t)) \sin(\phi_{A,UAV/SB/Ship}(t)) \\ \sin(\phi_{E,UAV/SB/Ship}(t)) \end{bmatrix}^T \end{aligned} \quad (15)$$

where  $\phi_{A,UAV/SB/Ship}(t)$  and  $\phi_{E,UAV/SB/Ship}(t)$  denote for the azimuth and elevation angles of UAV, single-cluster, and ship along the moving direction, respectively. The above angles are time-variant with the azimuth and elevation angular speed  $\omega_{A,UAV/SB/Ship}$  and  $\omega_{E,UAV/SB/Ship}$ .

–In the MB case

For the MB components, the channel coefficient  $h_{pq,kl_k}^{MB}(t)$  can be expressed as

$$\begin{aligned} h_{pq,nm_n}^{MB}(t) &= \begin{bmatrix} F_{p,V}^T(\alpha_{pT,nm_n}^{MB}(t), \beta_{pT,nm_n}^{MB}(t)) \\ F_{p,H}^T(\alpha_{pT,nm_n}^{MB}(t), \beta_{pT,nm_n}^{MB}(t)) \end{bmatrix}^T \\ &\begin{bmatrix} \sqrt{\kappa_{n,m_n}^{-1}} e^{j\Theta_{n,m_n}^{VV}} & e^{j\Theta_{n,m_n}^{HV}} \\ e^{j\Theta_{n,m_n}^{HV}} & \sqrt{\kappa_{n,m_n}^{-1}} e^{j\Theta_{n,m_n}^{VV}} \end{bmatrix} \\ &\begin{bmatrix} F_{q,V}^R(\alpha_{qR,nm_n}^{MB}(t), \beta_{qR,nm_n}^{MB}(t)) \\ F_{q,H}^R(\alpha_{qR,nm_n}^{MB}(t), \beta_{qR,nm_n}^{MB}(t)) \end{bmatrix} e^{j\varphi_{nm_n}^{MB}} \\ &\times e^{j2\pi \int_0^t (f_{pT,nm_n}^{MB}(t) + f_{qR,nm_n}^{MB}(t)) dt} \\ &\times e^{j\frac{2\pi}{\lambda} (\mathbf{d}_p^T(t) \cdot \mathbf{M}_V^T(t) \cdot \Phi_{pT,nm_n}^{MB}(t) + \mathbf{d}_q^R(t) \cdot \mathbf{M}_V^R(t) \cdot \Phi_{qR,nm_n}^{MB}(t))} \end{aligned} \quad (16)$$

where  $\Phi_{pT(qR),nm_n}^{MB}(t)$  denotes the time-variant AoDs/AoAs vector between the  $m_n$ th scatterer in the  $n$ th twin-cluster pair and Tx/Rx,  $f_{pT,nm_n}^{MB}(t)$  denotes the time-variant Doppler frequency caused by the movements of UAV and first bounce  $C_{n,A}$  of twin-cluster, and  $f_{qR,nm_n}^{MB}(t)$  denotes the time-variant Doppler frequencies causing by the movements of ship and last bounce  $C_{n,Z}$  of twin-cluster.  $\kappa_{n,m_n}^{-1}$  is the cross polarization power ratio. The expressions of  $\Phi_{pT(qR),nm_n}^{MB}(t)$ ,  $f_{pT,nm_n}^{MB}(t)$ , and  $f_{qR,kl_k}^{MB}(t)$  are given as

$$\Phi_{pT(qR),nm_n}^{MB}(t) = \begin{bmatrix} \cos(\beta_{pT(qR),nm_n}^{MB}(t)) \cos(\alpha_{pT(qR),nm_n}^{MB}(t)) \\ \cos(\beta_{pT(qR),nm_n}^{MB}(t)) \sin(\alpha_{pT(qR),nm_n}^{MB}(t)) \\ \sin(\beta_{pT(qR),nm_n}^{MB}(t)) \end{bmatrix}^T \quad (17)$$

$$f_{pT, nm_n}^{\text{MB}}(t) = \frac{\langle \mathbf{D}_{pT, nm_n}^{\text{MB}}(t), \mathbf{v}^{\text{UAV}}(t) - \mathbf{v}_{\text{CA}}^{\text{MB}}(t) \rangle}{\lambda \|\mathbf{D}_{pT, nm_n}^{\text{MB}}(t)\|} \quad (18)$$

$$f_{qR, nm_n}^{\text{MB}}(t) = \frac{\langle \mathbf{D}_{qR, nm_n}^{\text{MB}}(t), \mathbf{v}^{\text{Ship}}(t) - \mathbf{v}_{\text{CZ}}^{\text{MB}}(t) \rangle}{\lambda \|\mathbf{D}_{qR, nm_n}^{\text{MB}}(t)\|} \quad (19)$$

where

$$\mathbf{v}_{\text{CA/CZ}}^{\text{MB}}(t) = \left| \mathbf{v}_{\text{CA/CZ}}^{\text{MB}}(t) \right| \begin{bmatrix} \cos(\phi_{E, \text{CA/CZ}}^{\text{MB}}(t)) \cos(\phi_{A, \text{CA/CZ}}^{\text{MB}}(t)) \\ \cos(\phi_{E, \text{CA/CZ}}^{\text{MB}}(t)) \sin(\phi_{A, \text{CA/CZ}}^{\text{MB}}(t)) \\ \sin(\phi_{E, \text{CA/CZ}}^{\text{MB}}(t)) \end{bmatrix}^{\text{T}} \quad (20)$$

$$\mathbf{D}_{pT, nm_n}^{\text{MB}}(t) = \mathbf{D}_{pT, nm_n}^{\text{MB}}(t_0) + \mathbf{D}_{\text{CA}}^{\text{MB}}(t) - \mathbf{D}^{\text{UAV}}(t) \quad (21)$$

$$\mathbf{D}_{qR, nm_n}^{\text{MB}}(t) = \mathbf{D}_{qR, nm_n}^{\text{MB}}(t_0) + \mathbf{D}_{\text{CZ}}^{\text{MB}}(t) - \mathbf{D}^{\text{Ship}}(t) \quad (22)$$

$$\mathbf{D}_{\text{CA/CZ}}^{\text{MB}}(t) = \int_0^t \mathbf{v}_{\text{CA/CZ}}^{\text{MB}}(t) dt = \int_0^t \left( \mathbf{v}_{\text{CA/CZ}}^{\text{MB}}(t_0) + a_{\text{CA/CZ}}^{\text{MB}} \cdot t \right) dt. \quad (23)$$

Here,  $\mathbf{v}_{\text{CA/CZ}}^{\text{MB}}(t)$  denotes the speed vector of twin-cluster  $C_{n,A}/C_{n,Z}$ . The angles  $\phi_{A, \text{CA/CZ}}^{\text{MB}}(t)$  and  $\phi_{E, \text{CA/CZ}}^{\text{MB}}(t)$  stand for the azimuth and elevation angles of twin-cluster  $C_{n,A}/C_{n,Z}$  along the moving directions. Moreover,  $\mathbf{D}_{pT, nm_n}^{\text{MB}}(t)$  denotes the time-variant distance vector from the  $p$ th Tx antenna element to the  $n$ th first bounce cluster via  $m_n$ th ray, and  $\mathbf{D}_{qR, nm_n}^{\text{MB}}(t)$  denotes the time-variant distance vector from the  $n$ th last bounce cluster via  $m_n$ th ray to the  $q$ th Rx antenna element.

Based on the proposed theoretical model, the simulation model can be established by discretizing the angles. In the simulation model, all the angle parameters including the AoAs and EoAs, are obtained by adopting the method of equal area (MEA), and the remaining parameters are same with those of theoretical model.

### B. The Cluster Description of Sea Surface Fluctuation

For the maritime communication channel modeling, the single-cluster model is considered to describe scatterers distribution of sea surface. Due to the fluctuation of sea water, the sea surface presents different states at different time  $t$ . The scatterers distribution is closely related to the states of sea surface. Thus, the cluster description of sea surface fluctuation is crucial. Here, we use the summation model of multi-directional irregular sea to describe the sea surface fluctuation [37]. During the channel modeling, it is assumed that several clusters are randomly produced at initial moment. The  $x - y$  plane can be seen as the plane of sea at rest state, and the  $z$ -axis is pointing up. The initial coordinate of selected cluster is set as  $(x(t_0), y(t_0), z(t_0))$ , and the moving speed of sea wave (i.e. the speed of cluster in SB case) is assumed

as  $v^{\text{SB}}(t)$ . After time  $t$ , the position coordinate of the cluster is denoted by  $(x(t), y(t), z(t))$ . The values of  $x(t)$  and  $y(t)$  can be computed respectively as

$$x(t) = x(t_0) + v_x^{\text{SB}}(t) \cdot t \quad (24)$$

$$y(t) = y(t_0) + v_y^{\text{SB}}(t) \cdot t. \quad (25)$$

Moreover, the sea wave equation is superposition of different amplitudes, incident angles, and angular frequencies, which can be expressed as

$$z(t) = \sum_{s=1}^S a_s \cos(\omega_{s0}t - k_{s0} [x(t) \cos \theta_s + y(t) \sin \theta_s] + \varepsilon_s) \quad (26)$$

where  $k_{s0}$  denotes the wave number,  $\varepsilon_s$  is the random phase angles following the uniform distribution,  $a_s$  denotes the plane wavefronts of amplitude, and  $\theta_s$  denotes the angle of incidence from a range of directions.

### C. The Waveguide Effect in Maritime Scenarios

Due to the effect of atmospheric refraction over sea, the propagation of electromagnetic wave in the atmosphere will result in the waveguide effect. The atmospheric ducts in maritime environments can be classified into three main types: surface-based duct, elevated duct, and evaporation duct. Evaporation duct generally occurs in the sea surface atmosphere below the height of 40 m and has high probability of occurrence. In contrast, elevated duct height is usually between 600 m and 3000 m. These two kinds of ducts have great influences on signal transmissions in the UAV-to-ship communication links and can improve the over-sea UAV communications. Thus, how to describe the waveguide effect accurately is crucial [38]. Here, several ducting effects are assumed to abstract as unified waveguide effect, which is commonly caused by the decrease of water vapor concentration or the increase of temperature over the sea surface. The received signals will experience multiple reflections during the propagation. In the twin-cluster case, the signal propagation channel between clusters  $A$  and  $Z$  is abstracted as a rectangle cross section waveguide [39] as shown in Fig. 3. The origin coordinate system is set at the center of cross section. The coordinate of cluster  $A$  is denoted by  $(x_{\text{CA}}(t), y_{\text{CA}}(t), z_{\text{CA}}(t))$ , and the coordinate of cluster  $Z$  is denoted by  $(x_{\text{CZ}}(t), y_{\text{CZ}}(t), z_{\text{CZ}}(t))$ .  $I_{r_h, r_v}$  means that the ray experiences  $r_v$  times reflection from vertical plane and  $r_h$  times reflection from horizontal plane. The distance between  $I_{r_h, r_v}$  and the cluster  $Z$  can be expressed as

$$d_{r_h, r_v}(t) = \sqrt{(d_{r_h, r_v}^x(t))^2 + (d_{r_h, r_v}^y(t))^2 + (d_{r_h, r_v}^z(t))^2} \quad (27)$$

$$d_{r_h, r_v}^x(t) = \begin{cases} 2ar_h + x_{\text{CA}}(t) - x_{\text{CZ}}(t), & r_h \text{ is even} \\ 2ar_h - x_{\text{CA}}(t) - x_{\text{CZ}}(t), & r_h \text{ is odd} \end{cases} \quad (28)$$

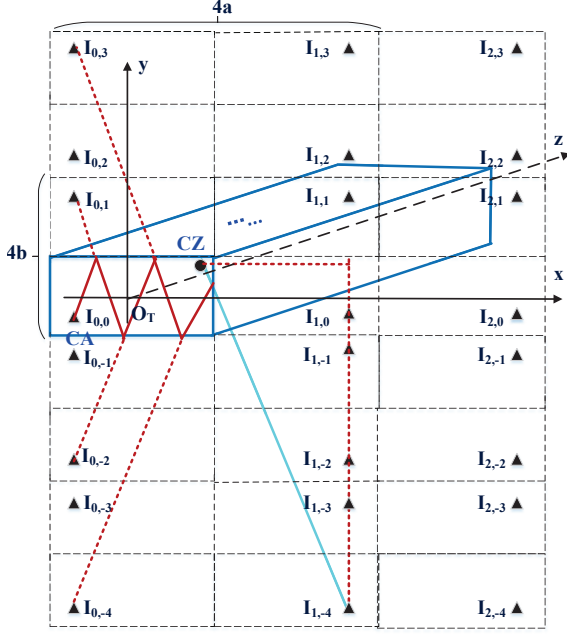


Fig. 3. The set of reflections in the excitation plane of sea waveguide.

$$d_{r_h, r_v}^y(t) = \begin{cases} 2br_v + y_{CA}(t) - y_{CZ}(t), & r_v \text{ is even} \\ 2br_v - y_{CA}(t) - y_{CZ}(t), & r_v \text{ is odd} \end{cases} \quad (29)$$

$$d_{r_h, r_v}^z(t) = z_{CA}(t) - z_{CZ}(t) \quad (30)$$

where  $2a$  and  $2b$  denote the width and height of an equivalent rectangle, respectively. The delay  $\tau_{wg}(t)$  between  $C_{n,A}$  and  $C_{n,Z}$  can be obtained by the computed distance  $d_{r_h, r_v}(t)$ .

#### D. Cluster Evolutions in SB and MB Cases

For the proposed UAV-to-ship channel model, all the parameters are time-variant, which bring the non-stationarities of channel model. In the non-stationary scenario, clusters can exist only a certain time period. Within this period, the clusters can be seen as static, and after this period, some clusters may appear or disappear [40]. To better describe this process, cluster evolutions in different domains are introduced [41].

In the SB case, the reflections happen due to the fluctuation of rough sea surface. The sea surface will change with time  $t$ . Here, we consider to use the birth-death process to describe the cluster evolution. At first, several clusters are generated at initial time  $t_0$ . Once the positions of initial clusters are determined, all the parameters can be obtained. Different parameters are randomly generated by following certain distributions. Then, the channel sampling intervals should be chosen in different domains, including  $\Delta t_e$  in time domain,  $\Delta x_e$  in space domain, and  $\Delta f_e$  in frequency domain. The clusters need to be updated during the different domains, and the birth-death process of clusters happens.

Some clusters survive with the probability  $P_{sur}(\Delta t_e, \Delta x_e, \Delta f_e)$ , which can be calculated refer to the method in [42]. By using the survival probability, the number of newly generated clusters can be calculated as

$$E[N_{new}(t + \Delta t_e, x + \Delta x_e, f + \Delta f_e)] = \frac{\lambda_G}{\lambda_R} (1 - P_{sur}(\Delta t_e, \Delta x_e, \Delta f_e)). \quad (31)$$

Here,  $\lambda_G$  and  $\lambda_R$  denote the birth and death rate respectively. Finally, the parameters information of survival and newly generated clusters needs to be accordingly updated.

In the MB case, a series of cluster pairs can be generated initially. Between the first bounce and last bounce clusters, the waveguide effect needs to be considered to describe the propagation path. After certain time/space/frequency period, some cluster pairs appear or disappear, which can be depicted by the birth-death process [42]. The process of cluster evolution in the MB case is similar with those in the SB case. The related channel parameters are randomly generated and updated by following specific distributions. The distances of first and last bounces are produced by the exponential distribution, the delays of rays within cluster pairs are assumed to follow exponential distribution, and the angular parameters are acquired using Wrapper Gaussian distribution.

### III. THE STATISTICAL PROPERTIES OF PROPOSED CHANNEL MODEL

Based on the proposed channel model, some typical channel statistical properties can be derived.

#### A. Local ST CF

The location space-time (ST) correlation function (CF) of two arbitrary CIRs  $h_{pq}^{tot}(t, \tau)$  and  $h_{p'q'}^{tot}(t - \Delta t, \tau)$  is defined as

$$\begin{aligned} R_h(t, \tau, \Delta t, \Delta x_T, \Delta x_R) &= E[h_{pq}^{tot}(t, \tau) h_{p'q'}^{tot*}(t - \Delta t, \tau)] \\ &= R_h^{LoS}(t, \Delta t, \Delta x_T, \Delta x_R) \delta(\tau - \tau^{LoS}(t)) \\ &\quad + R_h^{SB}(t, \Delta t, \Delta x_T, \Delta x_R) \delta(\tau - \tau_k^{SB}(t)) \\ &\quad + R_h^{MB}(t, \Delta t, \Delta x_T, \Delta x_R) \delta(\tau - \tau_n^{MB}(t)). \end{aligned} \quad (32)$$

Here, the local ST CFs can be calculated by the summation of LoS, SB, and MB components, which are assumed to be independent with each other. The detailed ST CFs can be rewritten as

$$\begin{aligned} R_h^{LoS}(t, \Delta t, \Delta x_T, \Delta x_R) &= h_{pq}^{LoS}(t) h_{p'q'}^{LoS*}(t - \Delta t) \\ &= e^{j2\pi(\Gamma_{pq}^{LoS}(t) - \Gamma_{p'q'}^{LoS}(t - \Delta t))} \end{aligned} \quad (33)$$

$$\begin{aligned} R_h^{SB}(t, \Delta t, \Delta x_T, \Delta x_R) &= h_{pq,kl_k}^{SB}(t) h_{p'q',kl_k}^{SB*}(t - \Delta t) \\ &= \sum_{k=1}^{K(t)} \sum_{l_k=1}^{L_k} e^{j2\pi(\Gamma_{pq,k}^{SB}(t) - \Gamma_{p'q',k}^{SB}(t - \Delta t))} \end{aligned} \quad (34)$$

$$\begin{aligned}
 R_h^{\text{MB}}(t, \Delta t, \Delta x_T, \Delta x_R) &= h_{pq, nm_n}^{\text{MB}}(t) h_{p'q', nm_n}^{\text{MB}*}(t - \Delta t) \\
 &= \sum_{n=1}^{N(t)} \sum_{m_n=1}^{M_n} e^{j2\pi(\Gamma_{pq,n}^{\text{MB}}(t) - \Gamma_{p'q',n}^{\text{MB}}(t - \Delta t))}
 \end{aligned} \quad (35)$$

where

$$\begin{aligned}
 \Gamma_{pq}^{\text{LoS}}(t) &= \int_0^t f_{pq}^{\text{LoS}}(t) dt \\
 &+ \frac{1}{\lambda} \left( \mathbf{d}_p^T(t) \mathbf{M}_V^T(t) \Phi_{\text{LoS}}^T(t) + \mathbf{d}_q^R(t) \mathbf{M}_V^R(t) \Phi_{\text{LoS}}^R(t) \right)
 \end{aligned} \quad (36)$$

$$\begin{aligned}
 \Gamma_{pq,k}^{\text{SB}}(t) &= \int_0^t \left( f_{pT,kl_k}^{\text{SB}}(t) + f_{qR,kl_k}^{\text{SB}}(t) \right) dt \\
 &+ \frac{1}{\lambda} \left( \mathbf{d}_p^T(t) \mathbf{M}_V^T(t) \Phi_{pT,kl_k}^{\text{SB}}(t) + \mathbf{d}_q^R(t) \mathbf{M}_V^R(t) \Phi_{qR,kl_k}^{\text{SB}}(t) \right)
 \end{aligned} \quad (37)$$

$$\begin{aligned}
 \Gamma_{pq,n}^{\text{MB}}(t) &= \int_0^t \left( f_{pT,nm_n}^{\text{MB}}(t) + f_{qR,nm_n}^{\text{MB}}(t) \right) dt \\
 &+ \frac{1}{\lambda} \left( \mathbf{d}_p^T(t) \mathbf{M}_V^T(t) \Phi_{pT,nm_n}^{\text{MB}}(t) + \mathbf{d}_q^R(t) \mathbf{M}_V^R(t) \Phi_{qR,nm_n}^{\text{MB}}(t) \right).
 \end{aligned} \quad (38)$$

1) *The spatial CCF*: By imposing  $\Delta t = 0$ , the time-variant spatial cross correlation function (CCF) between two arbitrary CIRs can be derived. The spatial CCF can be used to measure the spatial correlation of the UAV channel in the maritime scenarios. The LoS, SB, and MB components of spatial CCF are expressed as

$$\begin{aligned}
 r_h(t, \Delta x_T, \Delta x_R) &= \text{E} [h_{pq}^{\text{tot}}(t) h_{p'q'}^{\text{tot}*}(t)] \\
 &= r_h^{\text{LoS}}(t, \Delta x_T, \Delta x_R) + r_h^{\text{SB}}(t, \Delta x_T, \Delta x_R) \\
 &+ r_h^{\text{MB}}(t, \Delta x_T, \Delta x_R)
 \end{aligned} \quad (39)$$

where

$$r_h^{\text{LoS}}(t, \Delta x_T, \Delta x_R) = e^{j2\pi(\Gamma_{pq}^{\text{LoS}}(t) - \Gamma_{p'q'}^{\text{LoS}}(t))} \quad (40)$$

$$r_h^{\text{SB}}(t, \Delta x_T, \Delta x_R) = \sum_{k=1}^{K(t)} \sum_{l_k=1}^{L_k} e^{j2\pi(\Gamma_{pq,k}^{\text{SB}}(t) - \Gamma_{p'q',k}^{\text{SB}}(t))} \quad (41)$$

$$r_h^{\text{MB}}(t, \Delta x_T, \Delta x_R) = \sum_{n=1}^{N(t)} \sum_{m_n=1}^{M_n} e^{j2\pi(\Gamma_{pq,n}^{\text{MB}}(t) - \Gamma_{p'q',n}^{\text{MB}}(t))}. \quad (42)$$

2) *The temporal ACF*: By imposing  $\Delta x_T = 0$  and  $\Delta x_R = 0$ , the time-variant autocorrelation function (ACF) can be obtained. The temporal ACF can be used to measure the time correlation of the UAV channel in the maritime scenarios. The detailed expressions are as follows.

$$\begin{aligned}
 \rho_h(t, \Delta t) &= \text{E} [h_{pq}^{\text{tot}}(t) h_{pq}^{\text{tot}*}(t - \Delta t)] \\
 &= \rho_h^{\text{LoS}}(t, \Delta t) + \rho_h^{\text{SB}}(t, \Delta t) + \rho_h^{\text{MB}}(t, \Delta t)
 \end{aligned} \quad (43)$$

where

$$\rho_h^{\text{LoS}}(t, \Delta t) = e^{j2\pi(\Gamma_{pq}^{\text{LoS}}(t) - \Gamma_{pq}^{\text{LoS}}(t - \Delta t))} \quad (44)$$

$$\rho_h^{\text{SB}}(t, \Delta t) = \sum_{k=1}^{K(t)} \sum_{l_k=1}^{L_k} e^{j2\pi(\Gamma_{pq,k}^{\text{SB}}(t) - \Gamma_{pq,k}^{\text{SB}}(t - \Delta t))} \quad (45)$$

$$\rho_h^{\text{MB}}(t, \Delta t) = \sum_{n=1}^{N(t)} \sum_{m_n=1}^{M_n} e^{j2\pi(\Gamma_{pq,n}^{\text{MB}}(t) - \Gamma_{pq,n}^{\text{MB}}(t - \Delta t))}. \quad (46)$$

### B. The Doppler PSD

The Doppler power spectrum density (PSD) can be used to describe the averaged power distribution along the Doppler frequency. By the Fourier transform of time-variant ACF in regard to  $\Delta t$ , the time-variant Doppler PSD can be derived as

$$S_h(t, f_{DP}) = \int_{-\infty}^{\infty} \rho_h(t, \Delta t) e^{-j2\pi f_{DP} \Delta t} d\Delta t \quad (47)$$

where  $f_{DP}$  denotes the Doppler frequency. It is noted that the Doppler frequency is caused by the movements of UAV, ship, and clusters in the maritime scenarios.

### C. The Delay PSD

To describe the distribution of powers along the delays of rays, the time-variant delay PSD  $\Upsilon_{pq}(t, \tau)$  can be derived. The powers are acquired by the CIRs between the  $p$ th Tx antenna element and the  $q$ th Rx antenna element. The detailed expression of time-variant delay PSD can be expressed as

$$\begin{aligned}
 \Upsilon_{pq}(t, \tau) &= \sum_{k=1}^{K(t)} \sum_{l_k=1}^{L_k} \left| h_{pq,kl_k}^{\text{SB}}(t) \right|^2 \delta(\tau - \tau_{l_k}^{\text{SB}}(t)) \\
 &+ \sum_{n=1}^{N(t)} \sum_{m_n=1}^{M_n} \left| h_{pq,nm_n}^{\text{MB}}(t) \right|^2 \delta(\tau - \tau_{m_n}^{\text{MB}}(t)).
 \end{aligned} \quad (48)$$

### D. The Stationary Interval

The stationary interval means the maximum duration in which the channel statistics between different time instants can be seen as wide-sense stationary (WSS). It can be used to measure the time-variant channel characteristics of non-stationary UAV channel in maritime scenarios. Here, we use the method of local region of stationary (LRS) to calculate the stationary interval and depict the non-stationarity of channel. The stationary interval can be expressed as

$$T_s(t_d) = \min \{ \Delta t \mid c(t_d, \Delta t) < c_{\text{thresh}} \} \quad (49)$$

where  $c(t_d, \Delta t)$  denotes the calculated correlation coefficient, and  $c_{\text{thresh}}$  is a pre-determined threshold of correlation coefficient which is generally set as 80%. Here, the correlation coefficient of two averaged delay PSDs can be calculated as

$$c(t_d, \Delta t) = \frac{\int \bar{\Upsilon}_{pq}(t_d, \tau) \bar{\Upsilon}_{pq}(t_d + \Delta t, \tau) d\tau}{\max \left\{ \int \bar{\Upsilon}_{pq}(t_d, \tau)^2 d\tau, \int \bar{\Upsilon}_{pq}(t_d + \Delta t, \tau)^2 d\tau \right\}}. \quad (50)$$

The averaged delay PSDs can be expressed as

$$\bar{\Upsilon}_{pq}(t_d, \tau) = \frac{1}{N_P} \sum_d^{d+N_P-1} |h_{pq}^{tot}(t_d, \tau)|^2 \quad (51)$$

where  $t_d$  is the time of  $d$ th drop,  $N_P$  is the averaged delay PSDs number, and  $h_{pq}^{tot}(t_d, \tau)$  is the CIR.

#### IV. NUMERICAL RESULTS AND ANALYSIS

In this section, some key channel statistical properties of UAV-to-ship channel models have been studied. The variation of ST CF at different time instants represents the non-stationary property of the model in time domain. In Fig. 4, the temporal ACFs of the channel model are shown. During the simulations, all the parameters can be seen as time-variant, including the moving directions and speeds of Tx, Rx, and clusters between Tx and Rx. From this figure, the values of temporal ACFs are changed with time  $t$ , and the non-stationarity of UAV-to-ship channel can be described directly.

For the channel model, the NLoS components are consisted of the SB case and MB case. The SB components are introduced by the fluctuations of sea water. The moving speed of SB cluster is influenced by the wind speed across the sea surface. Thus, by changing the speed of SB cluster, the influence of severe weather on the UAV-to-ship channel propagations can be better described. Here, we mainly focus the studies of SB components of proposed channel model in normal weather, which assume the speed of SB cluster as 0.5 m/s. The description of sea water fluctuation can be obtained using the sea wave equation, which is given in Fig. 5(a). During the simulation, the initial positions of SB clusters are selected, and the clusters after time  $t$  can be derived according to the initial positions and wind speed. By instituting the coordinate values of UAV, ship, and SB cluster, the angle and distance parameters can be calculated. Then, the related local

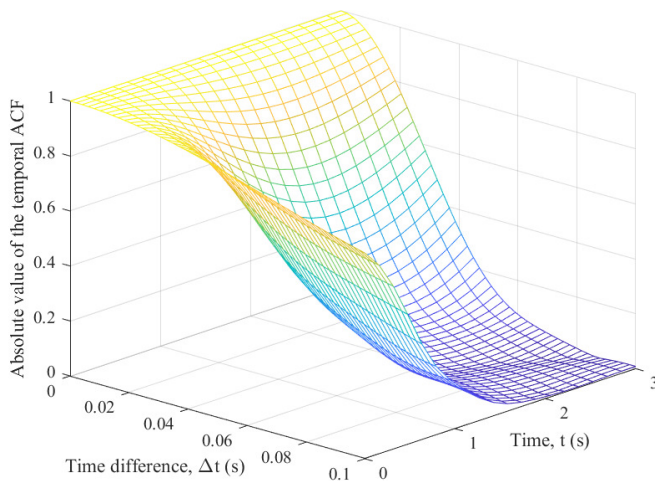


Fig. 4. Absolute value of the local 3D temporal ACFs of the non-stationary UAV-to-ship channel model ( $f_c = 5.5$  GHz,  $v^{\text{UAV}} = 3$  m/s,  $a^{\text{UAV}} = 2$  m/s<sup>2</sup>,  $v^{\text{Ship}} = 5$  m/s,  $a^{\text{Ship}} = 0.5$  m/s<sup>2</sup>,  $v_{\text{CA}}^{\text{MB}} = v_{\text{CZ}}^{\text{MB}} = 0.5$  m/s).

temporal ACFs are further acquired. Here, we take one cluster as an example to analyze the influence of SB case channel model, and the related simulations using the analytical and simulation results can be observed in Fig. 5(b). The analytical results are acquired by the derivation of ACF, and the simulation results are obtained by the correlation of CIRs. From this figure, the analytical results of ACFs can provide a good match with the corresponding simulation results, which ensure the correctness of our derivations. Moreover, the moving speeds and the angular speeds of the Tx and Rx will have certain impacts on the values of ACFs. Different Tx/Rx speeds will result in different variation trends of ACFs. With the increasing of Tx/Rx speed, the decline of temporal ACFs becomes faster.

Fig. 6 provides the comparisons of the temporal ACFs in SB and MB cases at time  $t = 1$  s and  $t = 3$  s, respectively. From this figure, we can see that the analytical result can provide a good fit with the simulation results in a small time separation. Moreover, the values of temporal ACFs vary with time  $t$  in SB/MB case. Meanwhile, the ACFs also have different variation trends in SB and MB cases at same time  $t$ . With the passage of time  $t$ , the moving velocity of Tx/Rx with certain accelerated velocity increase correspondingly, and the temporal correlation decline faster.

Fig. 7 shows the local 3D spatial CCFs of the proposed UAV-to-ship channel model at Rx side. On the Rx side, the Rx is set as moving with an accelerated speed  $a^{\text{Ship}} = 0.5$  m/s<sup>2</sup> and angular speed  $\omega^{\text{Ship}} = \pi/5$ . The antenna spacing at Rx side is normalized in terms of the wavelength, and the antenna spacing at Tx side is set as 0. From this figure, we can observe the variations of spatial CCFs with time  $t$  and Rx antenna spacing due to the non-stationarity of UAV-to-ship channel.

Fig. 8 gives the spatial CCFs with different antenna rotation angular speeds  $\gamma_T$  and  $\gamma_R$  at different time  $t$ . From this figure, we can observe that the analytical results of CCFs can fit well with the corresponding simulation results, which indicates the accuracy of the related derivations and simulations. Moreover, the different antenna rotation angular speeds will introduce time-variant antenna angles of the UAV and ship. The variations of UAV/ship antenna rotation angles will influence the spatial correlation of UAV-to-ship channel. At same time instant, different antenna rotation angular speeds will bring different variation trends of CCFs, and at same antenna rotation angular speeds case, the antenna angles at different time instants will also influence the variation trends of CCFs.

Fig. 9 illustrates the Doppler PSD of the channel model with different velocities and moving directions of UAV at time  $t = 3$  s. The Doppler PSDs can be computed by the Fourier transform of ACFs. From this figure, the comparisons of averaged power distribution along the Doppler frequency can be observed at different cases. For the same moving direction and different moving speeds of UAV, the trends of the PSDs are different. Moreover, for the different moving directions and same moving speed of UAV, the PSDs are also varied with the Doppler frequency. That is because the moving direction and speed of UAV can influence

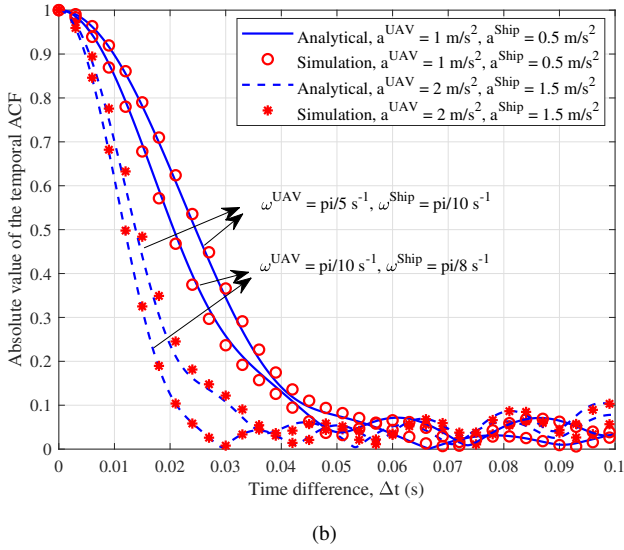
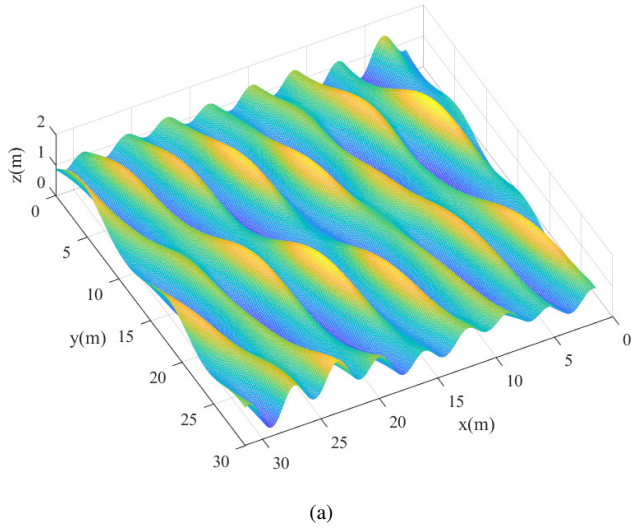


Fig. 5. (a) Descriptions of sea surface fluctuations at time  $t$ ; (b) Absolute values of the local temporal ACFs in SB case caused by sea surface fluctuation with different moving speeds and angular speeds of the Tx and Rx at time  $t$  ( $f_c = 5.5$  GHz,  $v^{\text{UAV}} = 3$  m/s,  $v^{\text{Ship}} = 5$  m/s,  $v^{\text{SB}} = 0.5$  m/s,  $t = 3$  s).

the values of AoDs, and the angular parameters will further affect the distribution of the PSDs.

In Fig. 10, the delay PSDs of the proposed UAV-to-ship channel model are exhibited. By instituting the ray delays and the corresponding powers within clusters, the twin-cluster delay PSDs can be obtained. Fig. 10 shows the power distributions along the delays at different waveguide sizes and reflection orders. The distance between the Tx and Rx is set as  $D_{TR} = 600$  m. The delay PSDs have different variation trends with waveguide sizes  $a = 20$  m and  $a = 40$  m. Moreover, the reflection orders will also have influences on the delay PSDs.

According to the waveguide effect mechanism, for longer distance between Tx and Rx, the smaller value of angular spread

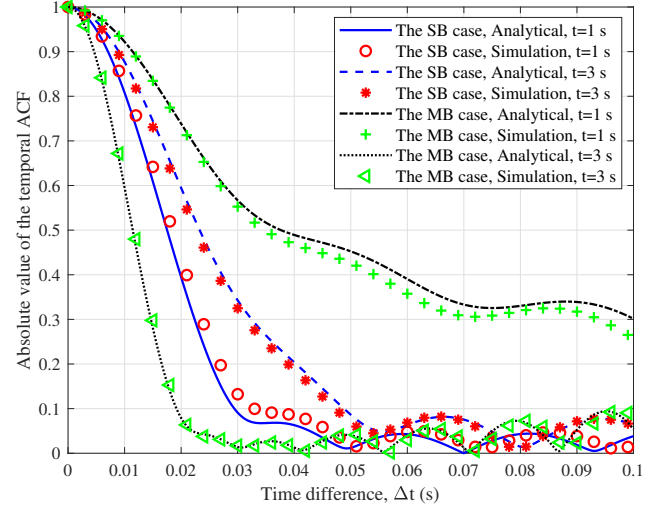


Fig. 6. Absolute values of the local temporal ACFs at different time instances in SB and MB cases ( $f_c = 5.5$  GHz,  $v^{\text{UAV}} = 3$  m/s,  $a^{\text{UAV}} = 2$  m/s<sup>2</sup>,  $v^{\text{Ship}} = 5$  m/s,  $a^{\text{Ship}} = 0.5$  m/s<sup>2</sup>,  $v_{\text{CA}}^{\text{MB}} = v_{\text{CZ}}^{\text{MB}} = 0.5$  m/s,  $v^{\text{SB}} = 0.5$  m/s).

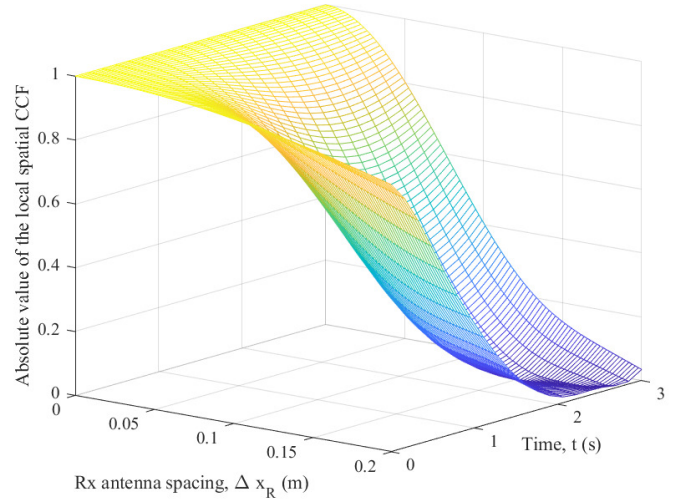


Fig. 7. Absolute value of the local 3D spatial CCFs of the non-stationary UAV-to-ship channel model ( $f_c = 5.5$  GHz,  $v^{\text{UAV}} = 3$  m/s,  $a^{\text{UAV}} = 2$  m/s<sup>2</sup>,  $\omega^{\text{UAV}} = \pi/10$ ,  $v^{\text{Ship}} = 5$  m/s,  $a^{\text{Ship}} = 0.5$  m/s<sup>2</sup>,  $\omega^{\text{Ship}} = \pi/5$ ).

is recommended in channel simulation, while the larger value of angular spread is recommended for the shorter distance between Tx and Rx. In Fig. 11, the angular PSD of the UAV-to-ship channel model is provided. It considers that 1 antenna is adopted at Tx and 128 antennas are employed at Rx. Here, the multiple signal classification algorithm is used to estimate the angular PSD. From this figure, we can observe the appearance and disappearance properties of clusters along the Rx array axis, which presents the birth and death process of clusters from the space domain. The variation of angular power spectrum represents the non-stationary property of the model in space domain.

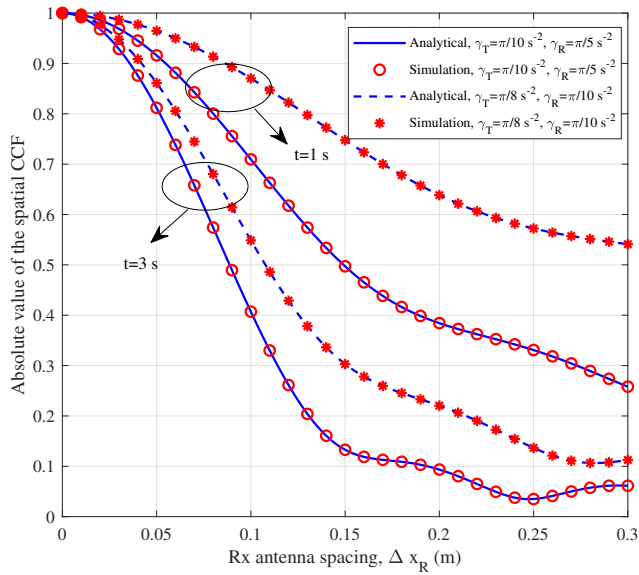


Fig. 8. Absolute value of the local spatial CCFs at different time instances and antenna rotation angles ( $f_c = 5.5$  GHz,  $v^{UAV} = 5$  m/s,  $a^{UAV} = 0$  m/s<sup>2</sup>,  $v^{Ship} = 3$  m/s,  $a^{Ship} = 0$  m/s<sup>2</sup>).

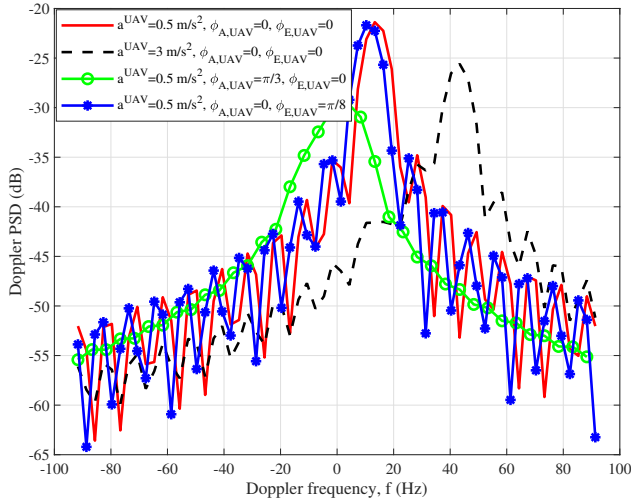


Fig. 9. The Doppler PSD of channel model with different velocities and moving directions of UAVs at time instant  $t = 3$  s ( $f_c = 5.5$  GHz,  $v^{UAV} = 3$  m/s,  $v^{Ship} = 5$  m/s,  $v^{SB} = 0.5$  m/s,  $H_T = 100$  m,  $H_R = 1.5$  m).

To study the non-stationarity of UAV-to-ship channels, the stationary intervals are illustrated. In Fig. 12, the empirical complementary CDFs of stationary intervals of our proposed channel model at different UAV speeds are given. By setting the UAV speeds as  $v^{UAV} = 1$  m/s, 5 m/s, and 10 m/s, the complementary CDFs are compared. We can notice that with the increasing of UAV speeds, the stationary intervals of UAV-to-ship channel will be reduced. Moreover, the UAV moves towards the ship side, and with the decrease of distance between the UAV and

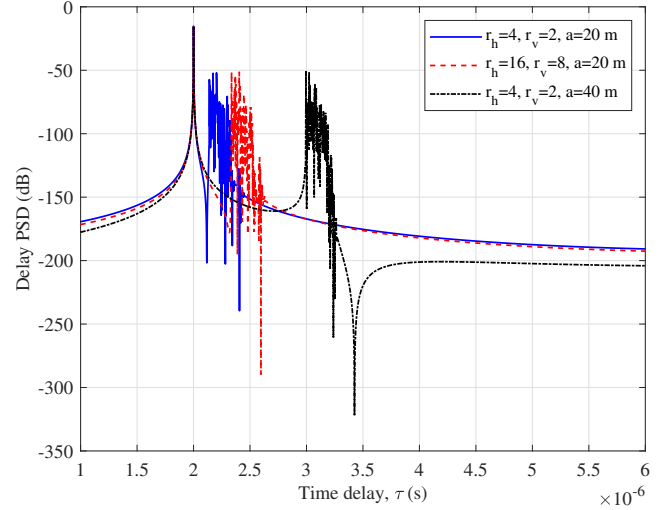


Fig. 10. The delay PSDs of the non-stationary UAV-to-ship channel model at different reflection orders and waveguide sizes ( $f_c = 5.0$  GHz,  $D_{TR} = 600$  m,  $\lambda_G = 20$ ,  $\lambda_R = 1$ ,  $v^{UAV} = 3$  m/s,  $v^{Ship} = 3$  m/s).

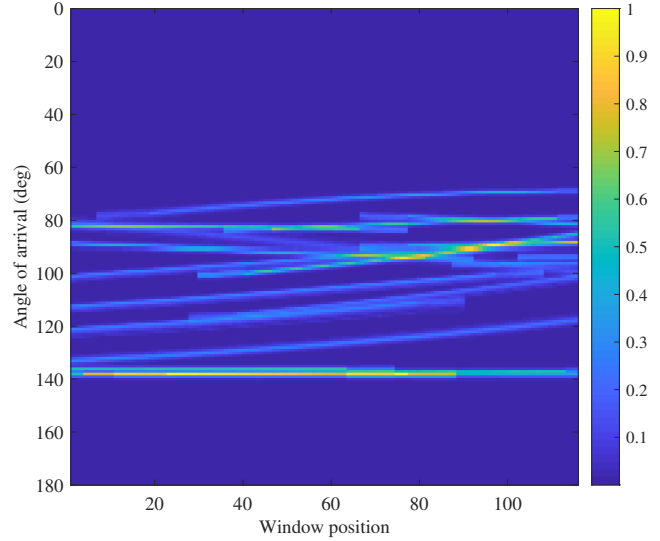


Fig. 11. The angular PSD of the non-stationary UAV-to-ship channel model ( $f_c = 5.0$  GHz,  $D_{TR} = 600$  m,  $\lambda_G = 20$ ,  $\lambda_R = 1$ ,  $v^{UAV} = 3$  m/s,  $v^{Ship} = 3$  m/s).

ship, the angular parameters change faster, which may influence the stationary interval.

Fig. 13 shows the root-mean-square (RMS) delay spreads for UAV-to ship channel model by considering the over-sea waveguide effect. The waveguide effect is an interesting propagation effect in the maritime scenario, and can act as “leaky waveguide” to reduce signal propagation attenuations [10]. To describe the over-sea waveguide effect, rectangular waveguide has been abstracted by introducing the reflection order  $\gamma_h$  from horizontal plane and  $\gamma_v$  from vertical plane. By adjusting the values of reflection orders, the comparison of RMS delay spreads

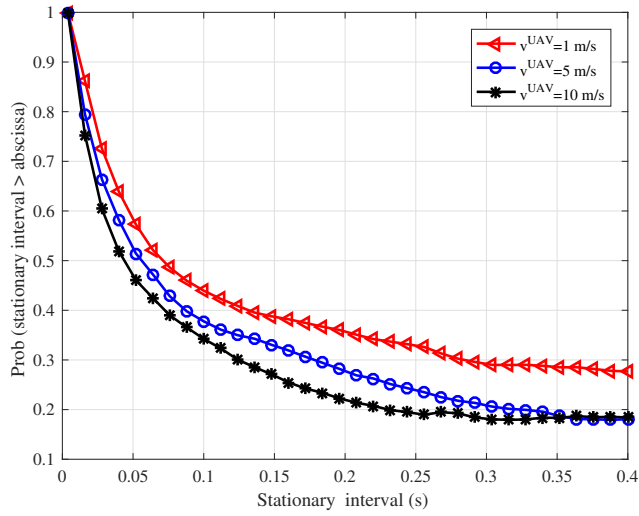


Fig. 12. Empirical CCDFs of stationary intervals for the non-stationary UAV-to-ship channel model ( $f_c = 5.5$  GHz,  $a^{\text{UAV}} = 5$  m/s<sup>2</sup>,  $v^{\text{Ship}} = 5$  m/s,  $a^{\text{Ship}} = 0.5$  m/s<sup>2</sup>,  $v_{\text{CA}}^{\text{MB}} = v_{\text{CZ}}^{\text{MB}} = 0.5$  m/s,  $t = 3$  s).

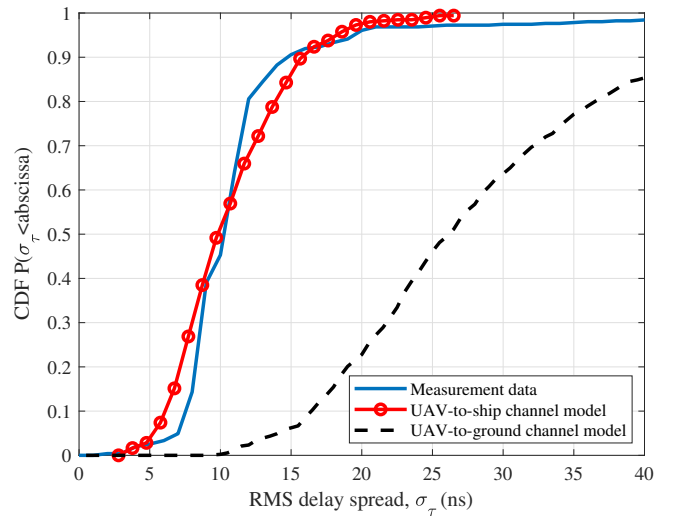


Fig. 14. The CDFs of RMS delay spreads for the proposed UAV-to-ship channel model, measurement data in [10], and UAV-to-ground channel model ( $f_c = 5.0$  GHz,  $\lambda_G = 20$ ,  $\lambda_R = 1$ ,  $\phi_{A,\text{Ship}} = \pi/5$ ,  $\phi_{E,\text{Ship}} = \pi/10$ ).

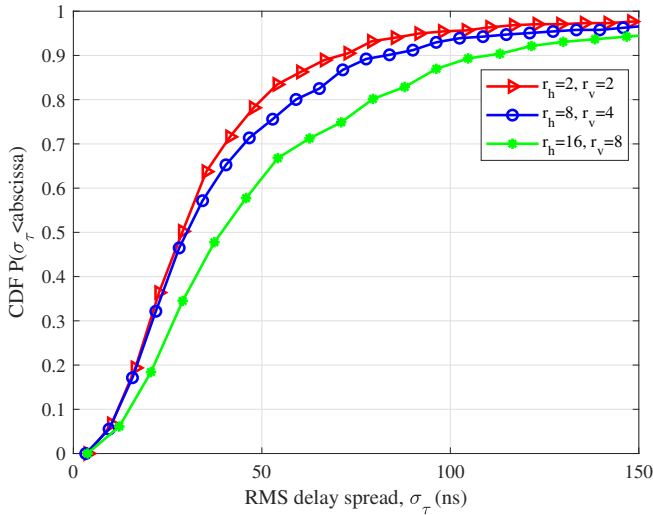


Fig. 13. The CDFs of RMS delay spreads for the non-stationary UAV-to-ship channel model considering waveguide effect ( $f_c = 5.5$  GHz,  $\lambda_G = 20$ ,  $\lambda_R = 1$ ,  $v^{\text{UAV}} = 3$  m/s,  $v^{\text{Ship}} = 3$  m/s).

for UAV-to-ship channel model has been illustrated. From this figure, we can observe that with the increasing of reflections orders, the RMS delay spread can be increased, that is in keeping with multiple reflections bring the higher RMS delay spreads. It is noted that the specific reflection orders need to be obtained by the related measurements.

To verify the proposed UAV-to-ship channel model, the RMS delay spread measurement data from [10] is used. The measurement campaigns were conducted with plane flying over the Pacific Ocean and measurement data at shorter link distances for higher elevation angles is selected. The measurement frequency is at C-

band (5030–5091 MHz). The field measurements were conducted by the help of the NASA Glenn’s S-3B aircraft carrying direct sequence spread spectrum (DS-SS) based channel sounder. The relative height between Tx and Rx ranges from 760 m to 785 m and the link distance is in the range of 0 m to 20000 m. More detailed measurement setup and aircraft trajectory can be found in [10]. Moreover, the UAV-to-ground channel model in [23] is used for comparisons. The CDFs of RMS delay spreads for the UAV-to-ship theoretical channel model, measurement data, and UAV-to-ground channel model are illustrated in Fig. 14. From this figure, we can observe that the UAV-to-ship theoretical model can fit well with the available over-sea setting measurement data, which validates the accuracy of our proposed model. Besides, compared with UAV-to-ground channels, it can be noticed that UAV-to-ship channels have smaller delay spread due to the sparse distribution of scatterers in the UAV-to-ship communication environments.

## V. CONCLUSIONS

In this paper, we have proposed a novel 3D non-stationary UAV-to-ship channel model, which considered the SB components caused by the rough sea surface and MB components introduced by over-sea waveguide effect in addition to the LoS component. The proposed model supports multi-mobility, including the arbitrary moving speeds and moving directions of UAV, ship, and clusters between the UAV and ship. All the parameters were set as time-variant to describe the non-stationarity of the UAV-to-ship channel. Based on the proposed model, some typical channel statistical properties have been derived and simulated, such as the temporal ACF, spatial CCF, Doppler PSD, delay PSD, angular PSD, stationary interval, and RMS delay spread. Results have shown that the analytical results can be verified by the simulation results in terms of ACFs and CCFs. A series

of time-variant statistical properties of the proposed model have been investigated to describe the non-stationarity of the UAV-to-ship channel. With the increase of the moving speed and the accelerated speed of UAV/ship, the temporal ACF declines faster. The change of UAV/ship antenna rotation angles led to different variation trends of spatial CCFs. Moreover, when the moving speed of UAV increases, the stationary interval will reduce by the fast changing of angular parameters. The RMS delay spreads have been analyzed using different reflection orders, which can reflect the influence of the waveguide effect. Finally, the RMS delay spread of the proposed UAV-to-ship channel model has been verified by the measurements.

## REFERENCES

- [1] Y. Zeng, R. Zhang, and T. J. Lim, "Wireless communications with unmanned aerial vehicles: opportunities and challenges," *IEEE Commun. Mag.*, vol. 54, no. 5, pp. 36–42, May 2016.
- [2] Y. Zeng, Q. Wu, and R. Zhang, "Accessing from the sky: a tutorial on UAV communications for 5G and beyond," in *Proceedings of the IEEE*, vol. 107, no. 12, pp. 2327–2375, Dec. 2019.
- [3] X.-H. You, C.-X. Wang, J. Huang, *et al.*, "Towards 6G wireless communication networks: vision, enabling technologies, and new paradigm shifts," *Sci. China Inf. Sci.*, vol. 64, no. 1, Jan. 2021.
- [4] C.-X. Wang, J. Huang, H. Wang, X. Gao, X.-H. You, and Y. Hao, "6G wireless channel measurements and models: trends and challenges," *IEEE Veh. Technol. Mag.*, accepted for publication.
- [5] L. Xie, J. Xu, and R. Zhang, "Throughput maximization for UAV-enabled wireless powered communication networks," *IEEE Int. Things J.*, vol. 6, no. 2, pp. 1690–1703, Apr. 2019.
- [6] W. Khawaja, I. Guvenc, D. W. Matolak, U. Fiebig, and N. Schneckenburger, "A survey of air-to-ground propagation channel modeling for unmanned aerial vehicles," *IEEE Commun. Surveys Tuts.*, vol. 21, no. 3, pp. 2361–2389, 3rd Quart., 2019.
- [7] C.-X. Wang, J. Bian, J. Sun, W. Zhang, and M. Zhang, "A survey of 5G channel measurements and models," *IEEE Commun. Surveys Tuts.*, vol. 20, no. 4, pp. 3142–3168, 4th Quart., 2018.
- [8] R. Amorim, H. Nguyen, P. Mogensen, I. Z. Kovcs, J. Wigard, and T. B. Srensen, "Radio channel modeling for UAV communication over cellular networks," *IEEE Wireless Commun. Lett.*, vol. 6, no. 4, pp. 514–517, Aug. 2017.
- [9] J. Huang, C.-X. Wang, H. Chang, J. Sun, and X. Gao, "Multi-frequency multi-scenario millimeter wave MIMO channel measurements and modeling for B5G wireless communication systems," *IEEE J. Sel. Areas Commun.*, vol. 38, no. 9, pp. 2010–2025, Sept. 2020.
- [10] D. W. Matolak and R. Sun, "Initial results for air-ground channel measurements & modeling for unmanned aircraft systems: Over-sea," in *Proc. IEEE AeroConf'14*, Big Sky, USA, Mar. 2014, pp. 1–15.
- [11] D. W. Matolak and R. Sun, "AG channel measurement and modeling results for over-sea conditions," *NASA Technical Report*, NASA/CR-2014-216674, June 2014.
- [12] D. W. Matolak and R. Sun, "Air-ground channel characterization for unmanned aircraft systems-Part I: Methods, measurements, and models for over-water settings," *IEEE Trans. Veh. Technol.*, vol. 66, no. 1, pp. 26–44, Jan. 2017.
- [13] R. Sun and D. W. Matolak, "Over-harbor channel modeling with directional ground station antennas for the air-ground channel," in *Proc. IEEE MILCOM'14*, Baltimore, USA, Oct. 2014, pp. 382–387.
- [14] K. Takizawa, F. Ono, M. Suzuki, H. Tsuji, and R. Miura, "Measurement on S-band radio propagation characteristics for unmanned aircraft systems," in *Proc. IEEE EuCAP'14*, The Hague, Netherlands, Apr. 2014, pp. 3068–3072.
- [15] Y. S. Meng and Y. H. Lee, "Measurements and characterizations of air-to-ground channel over sea surface at C-band with low airborne altitudes," *IEEE Trans. Veh. Technol.*, vol. 60, no. 4, pp. 1943–1948, May 2011.
- [16] Y. H. Lee and Y. S. Meng, "Analysis of ducting effects on air-to-ground propagation channel over sea surface at C-band," in *Proc. IEEE APMC'11*, Melbourne, USA, Dec. 2011, pp. 1678–1681.
- [17] W. Khawaja, O. Ozdemir, and I. Guvenc, "UAV air-to-ground channel characterization for mmWave systems," in *Proc. IEEE VTC'17-Fall*, Toronto, Canada, Sept. 2017, pp. 1–5.
- [18] N. X. Wang, X. F. Yin, X. S. Cai, R.-P. Jose, Y.-P. Antonio, and T. Li, "A novel air-to-ground channel modeling method based on graph model," in *Proc. IEEE EuCAP'19*, Krakow, Poland, Apr. 2019, pp. 1–5.
- [19] P. Xia, C. B. Chen, L. F. Huang, Z. Y. Shi, and Z. B. Gao, "Modeling of wireless channel between UAV and vessel using the FDTD method," in *Proc. IEEE WiCOM'14*, Beijing, China, Sept. 2014, pp. 100–104.
- [20] Z. Z. Cui, C. Briso-Rodriguez, K. Guan, C. Calvo-Ramirez, B. Ai, and Z. D. Zhong, "Measurement-based modeling and analysis of UAV air-ground channels at 1 and 4 GHz," *IEEE Antennas Wireless Propag. Lett.*, vol. 18, no. 9, pp. 1804–1808, Sept. 2019.
- [21] X. Cai *et al.*, "An empirical air-to-ground channel model based on passive measurements in LTE," *IEEE Trans. Veh. Technol.*, vol. 68, no. 2, pp. 1140–1154, Feb. 2019.
- [22] X. Cheng, Y. Li, C.-X. Wang, X. Yin, and D. W. Matolak, "A 3D geometry based stochastic model for unmanned aerial vehicle MIMO Ricean fading channels," *IEEE Int. Things J.*, vol. 7, no. 9, pp. 8674–8687, Sept. 2020.
- [23] H. Chang, C.-X. Wang, Y. Liu, J. Huang, J. Sun, W. Zhang, and X. Gao, "A novel non-stationary 6G UAV-to-ground wireless channel model with 3D arbitrary trajectory changes," *IEEE Int. Things J.*, DOI: 10.1109/JIOT.2020.3018479, Early Access, 2020.
- [24] H. Chang, J. Bian, C.-X. Wang, Z. Bai, W. Zhou, and H. Aggoune, "A 3D non-stationary wideband GBSM for low-altitude UAV-to-ground V2V MIMO channels," *IEEE Access*, vol. 7, no. 1, pp. 70719–70732, Dec. 2019.
- [25] Q. Wu, J. Xu, and R. Zhang, "Capacity characterization of UAV-enabled two-user broadcast channel," *IEEE J. Sel. Areas Commun.*, vol. 36, no. 9, pp. 1955–1971, Sept. 2018.
- [26] H. Jiang, Z. Zhang, L. Wu, and J. Dang, "Three-dimensional geometry-based UAV-MIMO channel modeling for A2G communication environments," *IEEE Commun. Lett.*, vol. 22, no. 7, pp. 1438–1441, July 2018.
- [27] H. Jiang, Z. Zhang, C.-X. Wang, J. Zhang, J. Dang, L. Wu, and H. Zhang, "A novel 3D UAV channel model for A2G communication environments using AoD and AoA estimation algorithm," *IEEE Trans. Commun.*, DOI: 10.1109/TCOMM.2020.3011716, Early Access, 2020.
- [28] M. T. Dabiri, S. M. S. Sadough, and M. A. Khalighi, "Channel modeling and parameter optimization for hovering UAV-based free-space optical links," *IEEE J. Sel. Areas Commun.*, vol. 36, no. 9, pp. 2104–2113, Sept. 2018.
- [29] Z. B. Gao, S. Q. Ke, C. B. Chen, and L. F. Huang, "Ray tracing based marine mobile wireless channel modeling," in *Proc. IEEE CCE'18-TW*, Taichung, Taiwan, May 2018, pp. 1–2.
- [30] Y. Y. Wu, Z. B. Gao, C. B. Chen, L. F. Huang, Y.-M. Huang, P. H. Chiang, and H. Sun, "Ray tracing based wireless channel modeling over the sea surface near Diaoyu islands," in *Proc. CCITSA'15*, Yilan, Taiwan, Dec. 2015, pp. 124–128.
- [31] R. He *et al.*, "Propagation channels of 5G millimeter wave vehicle-to-vehicle communications: Recent advances and future challenges," *IEEE Veh. Technol. Mag.*, vol. 15, no. 1, pp. 16–26, Mar. 2020.
- [32] L. Zhu, J. Zhang, Z. Xiao, X. Cao, X.-G. Xia, and R. Schober, "Millimeter-wave full-duplex UAV relay: joint positioning, beamforming, and power control," *IEEE J. Sel. Areas Commun.*, vol. 38, no. 9, pp. 2057–2073, Sept. 2020.
- [33] J. Bian, C.-X. Wang, J. Huang, Y. Liu, J. Sun, M. Zhang, and H. Aggoune, "A 3D wideband non-stationary multi-mobility model for vehicle-to-vehicle MIMO channels," *IEEE Access*, vol. 7, no. 1, pp. 32562–32577, Dec. 2019.
- [34] Q. Zhu, Y. Yang, C.-X. Wang, Y. Tan, J. Sun, X. Chen, and W. Zhong, "Spatial correlations of a 3D non-stationary MIMO channel model with 3D antenna arrays and 3D arbitrary trajectories," *IEEE Wireless Commun. Lett.*, vol. 8, no. 2, pp. 512–515, Apr. 2019.
- [35] Y. Liu, C.-X. Wang, J. Huang, J. Sun, and W. Zhang, "Novel 3-D nonstationary mmWave massive MIMO channel models for 5G high-speed train wireless communications," *IEEE Trans. Veh. Technol.*, vol. 68, no. 3, pp. 2077–2086, Mar. 2019.
- [36] S. Wu, C.-X. Wang, H. Aggoune, M. M. Alwakeel, and X. You, "A general 3D non-stationary 5G wireless channel model," *IEEE Trans. Commun.*, vol. 66, no. 7, pp. 3065–3078, July 2018.
- [37] E. R. Jefferys, "Directional seas should be ergodic," *Applied Ocean Research*, vol. 9, no. 4, pp. 186–191, 1987.
- [38] A. E. Forooshani, S. Bashir, D. G. Michelson, and S. Noghianian, "A survey of wireless communications and propagation modeling in underground mines," *IEEE Commun. Surveys Tuts.*, vol. 15, no. 4, pp. 1524–1545, 4th Quart., 2013.
- [39] Z. Sun and I. F. Akyildiz, "Channel modeling and analysis for wireless

networks in underground mines and road tunnels,” *IEEE Trans. Commun.*, vol. 58, no. 6, pp. 1758–1768, June 2010.

- [40] J. Bian, C.-X. Wang, X. Gao, X. You, and M. Zhang, “A general 3D non-stationary wireless channel model for 5G and beyond,” *IEEE Trans. Wireless Commun.*, DOI: 10.1109/TWC.2020.3047973, Early Access, 2021.
- [41] J. Wang, C.-X. Wang, J. Huang, H. Wang, and X. Gao, “A general 3D space-time-frequency non-stationary THz channel model for 6G ultra massive MIMO wireless communication systems,” *IEEE J. Sel. Areas Commun.*, DOI: 10.1109/JSAC.2021.3071850, Early Access, 2021.
- [42] Y. Liu, C.-X. Wang, and J. Huang, “Recent developments and future challenges in channel measurements and models for 5G and beyond high-speed train communication systems,” *IEEE Commun. Mag.*, vol. 57, no. 9, pp. 50–56, Sept. 2019.



**Yu Liu** received the Ph.D. degree in communication and information systems from Shandong University, Jinan, China, in 2017. From 2015 to 2017, she was a visiting scholar with the School of Engineering and Physical Sciences, Heriot-Watt University, Edinburgh, U.K.. From 2017 to 2019, she was a Postdoctoral Research Associate with the School of Information Science and Engineering, Shandong University, Jinan, China. Since 2019, she has been an Associate Professor with the School of Microelectronics, Shandong University, Jinan, China. Her main research interests include nonstationary

wireless MIMO channel modeling, high speed train wireless propagation characterization and modeling, and channel modeling for special scenarios.



**Cheng-Xiang Wang** (S’01-M’05-SM’08-F’17) received the BSc and MEng degrees in Communication and Information Systems from Shandong University, China, in 1997 and 2000, respectively, and the PhD degree in Wireless Communications from Aalborg University, Denmark, in 2004.

He was a Research Assistant with the Hamburg University of Technology, Hamburg, Germany, from 2000 to 2001, a Visiting Researcher with Siemens AG Mobile Phones, Munich, Germany, in 2004, and a Research Fellow with the University of Agder, Grimstad, Norway,

from 2001 to 2005. He has been with Heriot-Watt University, Edinburgh, U.K., since 2005, where he was promoted to a Professor in 2011. In 2018, he joined the National Mobile Communications Research Laboratory, Southeast University, China, as a Professor. He is also a parttime professor with the Purple Mountain Laboratories, Nanjing, China. He has authored four books, three book chapters, and more than 410 papers in refereed journals and conference proceedings, including 24 Highly Cited Papers. He has also delivered 22 Invited Keynote Speeches/Talks and 7 Tutorials in international conferences. His current research interests include wireless channel measurements and modeling, 6G wireless communication networks, and applying artificial intelligence to wireless networks.

Prof. Wang is a member of the Academia Europaea, a fellow of the IET, an IEEE Communications Society Distinguished Lecturer in 2019 and 2020, and a Highly-Cited Researcher recognized by Clarivate Analytics in 2017-2020. He is currently an Executive Editorial Committee member for the IEEE TRANSACTIONS ON WIRELESS COMMUNICATIONS. He has served as an Editor for nine international journals, including the IEEE TRANSACTIONS ON WIRELESS COMMUNICATIONS from 2007 to 2009, the IEEE TRANSACTIONS ON VEHICULAR TECHNOLOGY from 2011 to 2017, and the IEEE TRANSACTIONS ON COMMUNICATIONS from 2015 to 2017. He was a Guest Editor for the IEEE JOURNAL ON SELECTED AREAS IN COMMUNICATIONS, Special Issue on Vehicular Communications and Networks (Lead Guest Editor), Special Issue on Spectrum and Energy Efficient Design of Wireless Communication Networks, and Special Issue on Airborne Communication Networks. He was also a Guest Editor for the IEEE TRANSACTIONS ON BIG DATA, Special Issue on Wireless Big Data, and is a Guest Editor for the IEEE TRANSACTIONS ON COGNITIVE COMMUNICATIONS AND NETWORKING, Special Issue on Intelligent Resource Management for 5G and Beyond. He has served as a TPC Member, a TPC Chair, and a General Chair for more than 80 international conferences. He received 12 Best Paper Awards from IEEE GLOBECOM 2010, IEEE ICCT 2011, ITST 2012, IEEE VTC 2013-Spring, IWCMC 2015, IWCMC 2016, IEEE/CIC ICC 2016, WPMC 2016, WOCC 2019, IWCMC 2020, and WCSP 2020.



**Hengtai Chang** received the B.Sc. degree at School of Information Science and Engineering, Shandong University, Qingdao, China, in 2016. He is currently pursuing the Ph.D. degree at the School of Information Science and Engineering, Shandong University, Qingdao, China. His current research interests include UAV communications, wireless propagation channel measurements and channel modeling, and B5G/6G wireless communications.



**Yubei He** received the B.Sc. degree at the School of Information Science and Engineering, Shandong University, Qingdao, China, in 2017. She is currently pursuing the Ph.D. degree in Information and Communication Engineering from Shandong University, Qingdao, China. Her current research interests include maritime communications, wireless propagation channel measurements and channel modeling, and B5G/6G wireless communications.



**Ji Bian** received the B.Sc. degree in electronic information science and technology from Shandong Normal University, Jinan, China, in 2010, the M.Sc. degree in signal and information processing from Nanjing University of Posts and Telecommunications, Nanjing, China, in 2013, and the Ph.D. degree in information and communication engineering from Shandong University, Jinan, China, in 2019. From 2017 to 2018, he was a visiting scholar with the School of Engineering and Physical Sciences, Heriot-Watt University, Edinburgh, U.K. He is currently a lecturer with the School of

Information Science and Engineering, Shandong Normal University, Jinan, China. His research interests include 6G channel modeling and wireless big data.